





## RESEARCH LETTER

10.1029/2022GL100552

## Conditions for Convective Deep Inflow

Yi-Hung Kuo<sup>1,2</sup>  and J. David Neelin<sup>1</sup> 

<sup>1</sup>Department of Atmospheric and Oceanic Sciences, University of California, Los Angeles, CA, USA, <sup>2</sup>Now at Cooperative Institute for Modeling the Earth System, Program in Oceanic and Atmospheric Sciences, Princeton University, Princeton, NJ, USA

### Key Points:

- Observations and simulations point to a common structure of convective mass flux drawing air from a deep layer in the lower troposphere
- Most deep-convective precipitation comes from features with horizontal size comparable to or exceeding the lower-tropospheric depth
- For these, the nonlocal response of convective updrafts to buoyancy provides a simple explanation for the observed deep-inflow structure

### Supporting Information:

Supporting Information may be found in the online version of this article.

### Correspondence to:

Y.-H. Kuo,  
yhkuo@atmos.ucla.edu

### Citation:

Kuo, Y.-H., & Neelin, J. D. (2022). Conditions for convective deep inflow. *Geophysical Research Letters*, 49, e2022GL100552. <https://doi.org/10.1029/2022GL100552>

Received 26 JUL 2022

Accepted 5 OCT 2022

### Author Contributions:

**Conceptualization:** Yi-Hung Kuo, J. David Neelin  
**Formal analysis:** Yi-Hung Kuo, J. David Neelin  
**Funding acquisition:** J. David Neelin  
**Investigation:** Yi-Hung Kuo, J. David Neelin  
**Methodology:** Yi-Hung Kuo, J. David Neelin  
**Project Administration:** J. David Neelin  
**Resources:** J. David Neelin  
**Supervision:** J. David Neelin  
**Validation:** Yi-Hung Kuo  
**Visualization:** Yi-Hung Kuo  
**Writing – original draft:** Yi-Hung Kuo, J. David Neelin

**Abstract** Observations and cloud-resolving simulations suggest that a convective updraft structure drawing mass from a deep lower-tropospheric layer occurs over a wide range of conditions. This occurs for both mesoscale convective systems (MCSs) and less-organized convection, raising the question: is there a simple, universal characteristic governing the deep inflow? Here, we argue that nonlocal dynamics of the response to buoyancy are key. For precipitating deep-convective features including horizontal scales comparable to a substantial fraction of the troposphere depth, the response to buoyancy tends to yield deep inflow into the updraft mass flux. Precipitation features in this range of scales are found to dominate contributions to observed convective precipitation for both MCS and less-organized convection. The importance of such nonlocal dynamics implies thinking beyond parcel models with small-scale turbulence for representation of convection in climate models. Solutions here lend support to investment in parameterizations at a complexity between conventional and superparameterization.

**Plain Language Summary** Deep convection, whether in isolated thunderstorms or organized mesoscale convective systems, is a leading effect in climate dynamics and climate change, yet it remains subject to large uncertainties in climate models. The way that air enters convective clouds plays a substantial role in this uncertainty, and recently the importance of inflow through a deep layer in the lower troposphere has been noted, although why this should apply for both isolated and organized convection has been unclear. Here, we show that an aspect of dynamics omitted from conventional climate model representations provides a simple explanation for this for large clouds that account for most convective precipitation. This suggests physical effects requiring substantial revisions in climate models.

## 1. Introduction

Accurate simulation and forecasting of weather and climate depends on adequate representations of deep convection in general circulation models (GCMs). This remains a challenging subject (Kuo et al., 2020; Leung et al., 2022; Yano & Plant, 2020) even with recent advances in cloud-resolving models (CRMs) and machine learning (Bretherton et al., 2022; Wing et al., 2020). Challenges arise especially in regards to organized convection, such as mesoscale convective systems (MCSs; Moncrieff et al., 2012; Yano & Moncrieff, 2016) that account for a significant fraction of precipitation (Nesbitt et al., 2006). A major source of uncertainty is the entrainment process of environmental air entering in-cloud updrafts (Plant, 2010; Sherwood et al., 2014). The traditional view of entrainment assumes a plume/parcel rising from near the surface that is modified by its immediate surroundings via localized, small-scale turbulent mixing (Arakawa & Schubert, 1974). This motivated efforts to quantify a postulated local entrainment rate (Del Genio & Wu, 2010; Gregory, 2001; Masunaga & Luo, 2016; Siebesma et al., 2003)—primarily by indirect means—from which mass flux can be derived for plume models in parameterization schemes (de Rooy & Siebesma, 2010; Siebesma et al., 2007).

As schematized in Figure 1a, field measurements of deep-convective updrafts during aircraft campaigns (LeMone & Zipser, 1980; Lucas et al., 1994) and by radar wind profilers (Savazzi et al., 2021; Schiro et al., 2018), in accordance with CRM simulations (Li et al., 2008; Robe & Emanuel, 1996), identify a common mass flux structure that gradually increases throughout much of the lower troposphere. This dependence of mass flux on height, summarized in Figure 1b, is characteristic of both MCS and less-organized convection. It implies horizontal convergence of environmental air into the observed updraft through a deep layer in the lower troposphere. Such “deep-inflow” profiles are in general agnostic as to whether inflow occurs by spatially coherent flow, small-scale turbulence, or both. Contributions to this through coherent inflow are termed dynamic entrainment (Ferrier & Houze, 1989; Houghton & Cramer, 1951)—in contrast with the conventional paradigm of small-scale mixing.

© 2022 The Authors.

This is an open access article under the terms of the [Creative Commons Attribution-NonCommercial License](https://creativecommons.org/licenses/by/4.0/), which permits use, distribution and reproduction in any medium, provided the original work is properly cited and is not used for commercial purposes.

Writing – review & editing: Yi-Hung Kuo, J. David Neelin

Deep-inflow profiles can also be inferred from the dependence of precipitation on the temperature–moisture environment as a function of lower-tropospheric layer (Ahmed & Neelin, 2018).

Given the importance of mass flux in convective parameterizations, the occurrence of simple vertical structures warrants explanation, particularly since any potential for directly constraining such structures could aid in bypassing the elusive task of determining vertical dependence of entrainment rate (Kuang & Bretherton, 2006; Romps, 2010). The apparent widespread occurrence of deep-inflow structures, together with the surprising observation that such structures occur similarly for both MCS and less-organized deep convection, raises the question of whether there is some universal characteristic governing the dynamics of deep inflow.

Here, we adapt elements known in the anelastic modeling literature to show how they provide a straightforward explanation for this important physical phenomenon. As prelude, Section 2 previews the potential role of anelastic solutions and provides an observational analysis that indicates the range of horizontal scales in convective precipitation features. We then recap anelastic equations for the response to buoyancy, cast in a form suitable for vertical acceleration (Section 3), and show the implications for vertically nonlocal pressure/acceleration response. In Section 4, we examine response to horizontally localized buoyancy features while demonstrating robustness to smaller-scale variations. Finally, we discuss the conditions under which the nonlocal solution provides a simple explanation for deep inflow and implications for convective parameterizations based on parcel models that neglect these effects.

## 2. Convective Precipitation Feature Scales and Inflow

Complementing the overview in Figures 1a and 1b of the deep-inflow problem, key ingredients of the proposed solution are previewed in Figures 1c and 1d. We will argue that the response to buoyancy is nonlocal and tends to average over details of the flow and produce mass flux increasing with height in the lower troposphere—as in Figure 1c—for a range of reasonable conditions provided sufficiently large horizontal scales occur in the convective elements.

Figure 1d quantifies the claim that much of the deep-convective precipitation comes from features that include such horizontal scales. Contiguous features of convective precipitation are identified from satellite precipitation radar (PR) retrievals (Appendix A). The contribution to total convective precipitation is shown as a function of feature size estimated two different ways: by cord length of the feature and by square root of the area of the feature. The contribution to convective precipitation is further separated by features that meet common criteria for MCS, and less-organized features that do not. Note that stratiform precipitation is *not* included, since we wish to focus on the scales of features of the deep-convective precipitation. For both MCS and less-organized convection, the precipitation contribution peaks around 15 km, and >70% of the total convective rain is from events of this scale or greater for both feature size measures. That is, convective rain is mostly from deep-convective features whose horizontal extent is comparable to the depth of the troposphere. MCS features tend to have greater contribution to convective rain at large sizes than do less-organized features. While the conditionally averaged convective precipitation rate for less-organized features (squares) levels off as size exceeds ~25 km, the MCS precipitation rate (circles) continues to increase asymptotically as roughly the one-fourth power of size.

The convective precipitation region is not necessarily identical to that of the buoyancy, but provides a rough measure of the existence of strong updrafts and downdrafts indicative of buoyancy anomalies. The spatiotemporal coverage of the satellite PR provides regions and periods extensive enough to identify typical characteristics of convection. We also note that the PR resolution ~5 km coarse-grains smaller-scale variations, but suffices to support that localized features containing substantial convective rain occur over a broad range of scales. The robustness of the nonlocal effects discussed in Section 4 helps justify such coarse-graining.

We thus have (a) observational evidence that much of the convective rain in both MCS and less-organized systems comes from features with characteristic sizes of the convection exceeding ~10 km and (b) a theoretical basis for how the nonlocal nature of the response to buoyancy tends to yield deep inflow on such scales.

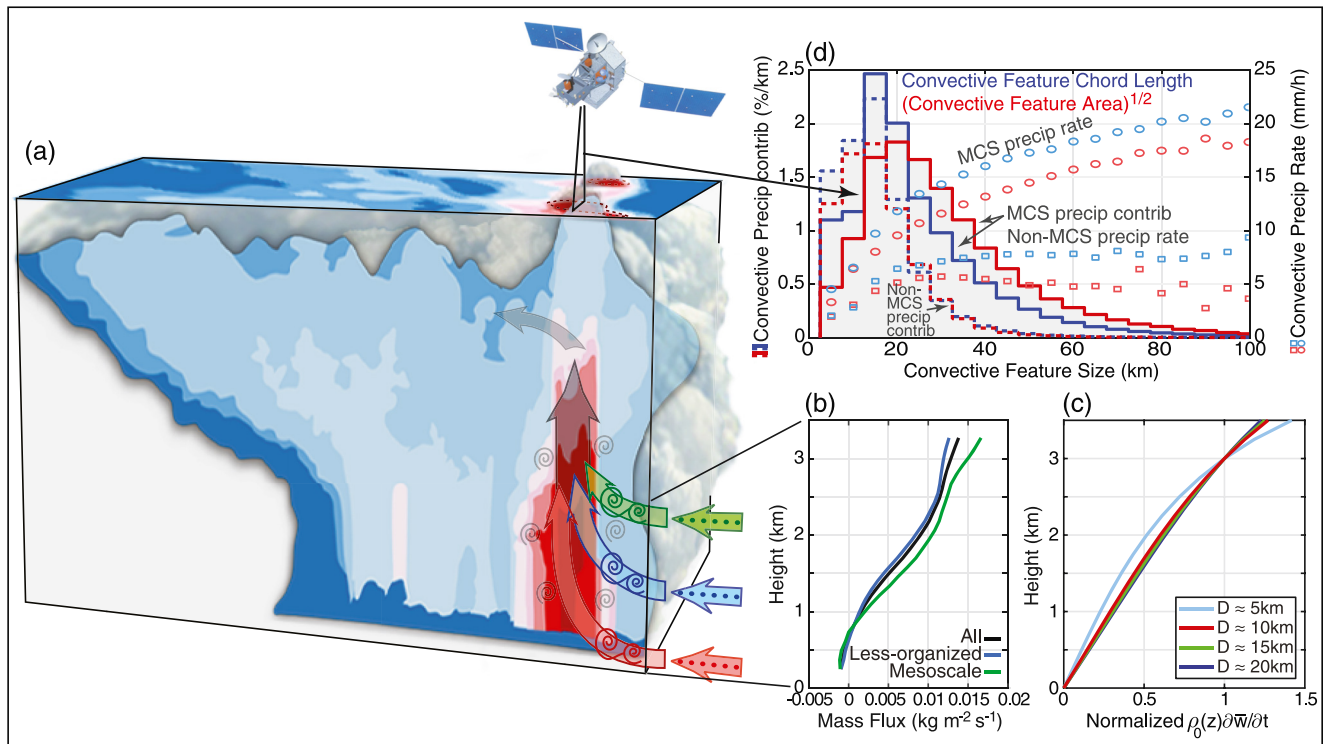


**Figure 1.** (a) Schematics showing (front view) the deep inflow of environmental air into convective clouds with lower-tropospheric layers all contributing substantially to the updraft through coherent flow and small-scale turbulence; (top view) satellite observations identifying convective precipitating features. (b) Mean deep-convective updraft mass flux profiles in the lower troposphere for mesoscale, less-organized, and all precipitating convective events estimated from radar wind profiler during the GOAmazon campaign adapted from Schiro et al. (2018). (c) Theoretical response of convective mass flux to complex buoyancy anomalies discussed in Section 4, as a preview of the robustness of the response in the lower troposphere, provided the characteristic horizontal scale  $D$  is sufficiently large. (d) Convective precipitation contribution (curves) and precipitation rate (markers), for mesoscale convective system (MCS) and non-MCS features, conditioned on convective feature size measured by chord length (blue) and square root of area (red); details in Appendix A. The areas under the MCS (solid) and non-MCS (dashed) precipitation contribution curves sum to unity. Feature size is solely based on contiguous convective precipitation pixels.

### 3. Anelastic Response to Buoyancy

We follow the anelastic framework (Ogura & Phillips, 1962) to derive the diagnostic equation for the response to buoyancy. The anelastic approximation assumes a horizontally homogeneous, time-invariant atmospheric density  $\rho_0(z)$ , allowing the governing system to filter acoustic waves and retain nonhydrostatic solutions relevant for deep convection with  $O(1)$  aspect ratio (Markowski & Richardson, 2011). Thus, the anelastic approximation has been widely adopted by CRMs (Bryan & Fritsch, 2002; Jung & Arakawa, 2008; Khairoutdinov & Randall, 2003).

#### 3.1. Nonlocal Response to Buoyancy Field

With vorticity and anelastic continuity equations, one can derive (see Section S1 in Supporting Information S1)

$$\nabla_h^2 a + \frac{\partial}{\partial z} \left[ \frac{1}{\rho_0} \frac{\partial}{\partial z} (\rho_0 a) \right] = \nabla_h^2 B + D, \quad (1)$$

where  $a \equiv \partial_t w$  is the Eulerian vertical acceleration,  $B$  the buoyancy, and  $D$  a quadratic function of spatial derivatives of velocity  $\mathbf{u}$  (i.e., associated with flow kinematics) that vanishes when  $\mathbf{u} \equiv 0$ . The influences of buoyancy and kinematics on  $a$  can thus be separately diagnosed. Here, we focus on the response to buoyancy, which allows a direct contrast to conventional parameterizations (Section S5 in Supporting Information S1).

In Equation 1, the operator acting on  $a$  is elliptic, one thus expects a global response even for localized forcing (Houze, 1993). The response is accompanied by adjustment to horizontal convergence driven by locally

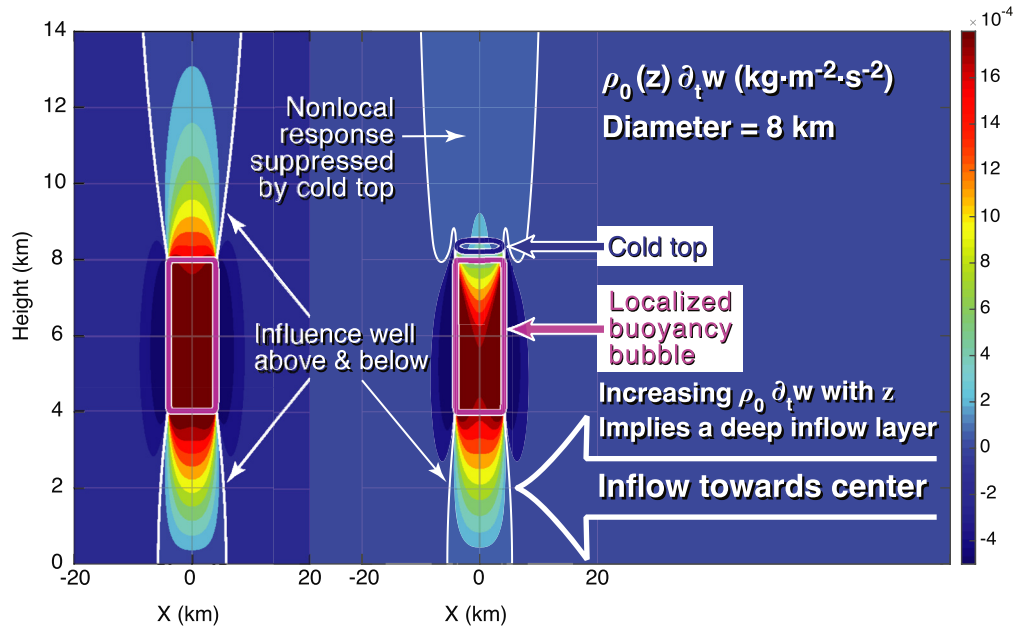


**Figure 2.** Cross section of vertical mass flux response (color shading;  $\text{kg}/\text{m}^2 \text{ s}^2$ ) to idealized buoyancy forcing with constant  $B = 0.01 \text{ m/s}^2$  in cylindrical bubbles of 8-km diameter (magenta contours). The case on the right also includes a negatively buoyant region immediately above ( $B = -0.06 \text{ m/s}^2$ ) to illustrate the tendency of the “convective cold-top” to cancel vertical motion above the main updraft. The white contours indicate zero response. The colorbar range is chosen to highlight details below the bubbles. See Sections S3 in Supporting Information S1 for numerical details and Section S5 in Supporting Information S1 for plume-model comparison.

hydrostatic pressure gradients (Jeevanjee & Romps, 2016; Peters, 2016) to ensure mass conservation. Note that buoyancy drives acceleration via  $\nabla_h^2 B$ —flow evolves following horizontal variation of buoyancy.

To give a concrete sense of the nonlocal dynamics, Figure 2 demonstrates two examples of the mass flux response field  $\rho_0 a$  (color shading) due to idealized cylindrical buoyancy bubbles of 8-km diameter (magenta contours). Here,  $a$  is from solving Equation 1 (with  $D \equiv 0$ ) for the two cases separately. The localized buoyancy generates strong upward acceleration within its diameter, accompanied by weak, broad downward acceleration in the surroundings. The extensive response reaches well below and above the bubble, driving a layer of flow into the convective region in the lower troposphere, contributing to the gradually increasing  $\rho_0 a$  with height, and outflow aloft from decreasing  $\rho_0 a$ . Other things equal, deeper bubbles generally result in greater response.

The nonlocal responses in Figure 2 result from the elliptic operator in Equation 1 and are well-known in principle (Cotton et al., 2010; Trapp, 2013). Interaction with the buoyancy can affect this: for example, if the upward velocity occurs above the region where latent heating can balance work against stratification, a negative buoyancy tendency will occur. This results in the convective cold-top phenomenon (Holloway & Neelin, 2007), with a region of negative buoyancy tending to cancel the response above, as illustrated on the right in Figure 2.

Here, we focus on the properties of the anelastic solution within and below the positively buoyant region. If this region is saturated (above an unstratified boundary layer), latent heating tends to cancel updraft negative buoyancy tendencies. When overall aspects of the buoyancy feature do not evolve rapidly, acceleration solutions (from small initial flow) constrain properties of updraft structure. Building on previous work, we can then ask under what conditions the nonlocal solutions might provide an explanation for the deep inflow and point to dynamics that might be missing from parcel models.

### 3.2. Analytic Monochromatic Vertical Structures

For a more detailed characterization of the nonlocal dynamics, we apply a Fourier transform to Equation 1:

$$-\frac{4\pi^2}{L^2} \hat{a} + \frac{\partial}{\partial z} \left[ \frac{1}{\rho_0} \frac{\partial}{\partial z} (\rho_0 \hat{a}) \right] = -\frac{4\pi^2}{L^2} \hat{B}, \quad (2)$$

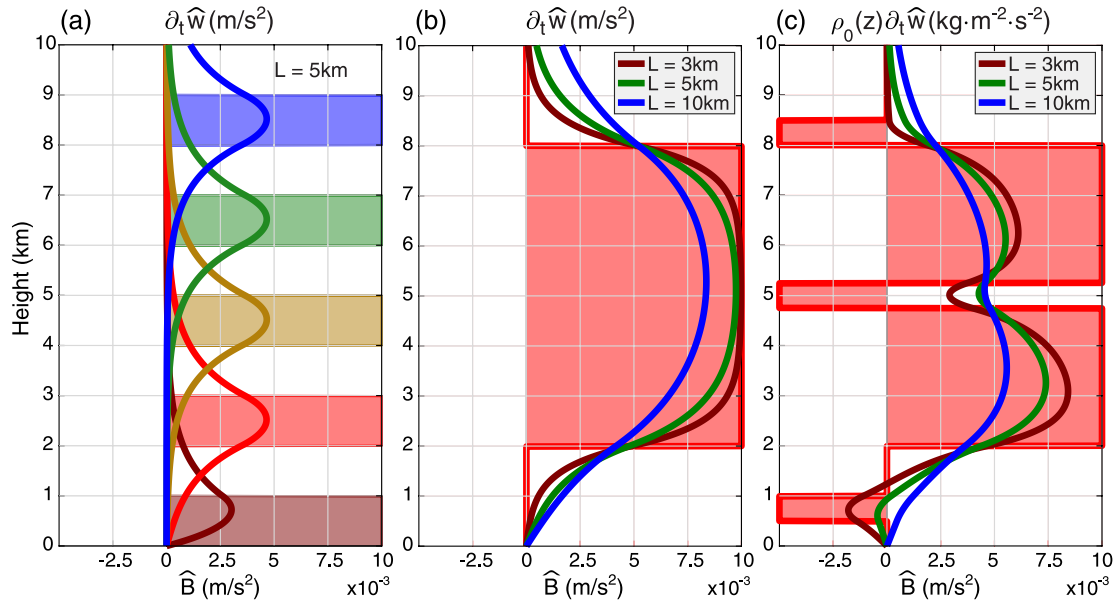


**Figure 3.** (a) Monochromatic solutions to Equation 2 of vertical acceleration response (lines) to individual buoyant layers located at different heights (shadings) with horizontal wavelength  $L = 5$  km. (b) As in (a), for a deeper layer (red) and varying  $L$ . (c) As in (b), with additional thin layers of negative buoyancy, for vertical mass flux response. See Section S2 in Supporting Information S1 for numerical details and Figures S2a and S2b in Supporting Information S1 for plume-model comparison.

where  $a \sim \hat{a}(z; k, \ell)e^{2\pi i(kx + \ell y)}$ ,  $B \sim \hat{B}(z; k, \ell)e^{2\pi i(kx + \ell y)}$ , and  $L \equiv (k^2 + \ell^2)^{-1/2}$  is the horizontal wavelength.

Consider a simple buoyancy structure with  $\hat{B}(z) \equiv \text{constant}$  within a layer and vanishing elsewhere—general profiles can be approximated by superposition. We can analytically solve Equation 2 (Section S2 in Supporting Information S1) for the homogeneous solutions:

$$\hat{a}^{\pm}(z; k, \ell) \sim e^{\pm 2\pi z/L}, \quad (3)$$

and for the particular solution within the buoyant layer:

$$\hat{a}^p(z; k, \ell) \approx \hat{B}(z; k, \ell). \quad (4)$$

The monochromatic (single-wavelength) solutions can then be constructed as a piecewise linear combination of  $\hat{a}^{\pm}$  and  $\hat{a}^p$  by matching across layer boundaries, yielding solutions similar to Jeevanjee (2017). Each horizontal wavelength gives rise to a vertical  $e$ -folding scale  $H_s \equiv L/2\pi$ —longer wavelength results in a greater range of nonlocal influence.

Figure 3a shows examples of  $\hat{a}$  (lines) given a buoyant layer of depth  $H_b = 1$  km and  $\hat{B} = 0.01$  m/s<sup>2</sup> (shadings) at various heights with  $L = 5$  km. Above the buoyancy, the vanishing condition requires that  $\hat{a} \sim e^{-2\pi z/L}$ . Below the buoyancy for layers away from the surface (compared with  $H_s$ ),  $\hat{a} \sim e^{+2\pi z/L}$ , and the overall profiles appear to be symmetric in  $z$  with maximum occurring in the middle of the layers. But for a layer at low altitude, the surface boundary condition results in  $\hat{a} \approx c_1 e^{+2\pi z/L} - c_2 e^{-2\pi z/L}$ —adding  $\hat{a}^p$  if the layer reaches the surface—causing an approximately linear dependence on height below the maximum as well as an overall weaker response magnitude. This surface control is generally important for sufficiently long wavelength (see also Figure 3b, blue line).

To further illustrate how the layer depth and horizontal wavelength affect the solutions, Figure 3b includes additional examples for a deeper layer of buoyancy ( $H_b = 6$  km; red) and varying  $L$ . Short wavelength ( $L/H_b \ll 1$ ) leads to limited nonlocal influence, mostly confined in the vicinity of the layer boundaries (brown line). Conversely, long wavelength and/or relatively shallow layer ( $L/H_b \gg 1$ ) would yield solutions extending well outside the buoyant layer with reduced magnitude (blue line; also contrast with Figure 3a). The aspect-ratio dependence is consistent with prior studies (Jeevanjee & Romps, 2016; Morrison, 2016), but there are other factors affecting the nonlocal behaviors. For deep-inflow applications,  $L$  relative to a typical distance from the

surface to the layer is important. Note also that the inflow can continue for a characteristic vertical scale  $\sim H_s$  within the buoyant layer. The mass flux responses corresponding to the accelerations in Figures 3a and 3b are similar but bottom-heavier since  $\rho_0$  decreases with height.

For a more sophisticated case, Figure 3c shows the mass flux responses  $\rho_0 \hat{a}$  (lines) to an idealized deep-convective structure with the addition of (a) a near-surface convective inhibition (CIN) layer; (b) a thin negatively buoyant layer representing, for example, effects of freezing/melting; and (c) a layer resembling the convective cold-top. The cold-top here is sufficient to limit the vertical extent of the acceleration for the shortest wavelength, but would have to be more intense for the longer wavelengths. Overall, the short-wavelength response tends to track the variation of buoyancy. For sufficiently large horizontal scales, the solution due to net-positive buoyancy has no difficulty tunneling through vertically restricted layers of negative buoyancy or near-surface CIN layer.

This last observation—based on a monochromatic argument but also supported by the solutions in Section 4—has practical implications. First, this helps understand why a nighttime CIN layer may not prevent preexisting storms from moving into a region, for example, over the Mississippi basin or the Amazon (Burleyson et al., 2016): the layer depth plus surface interactions limit the effect of CIN. This may also be relevant to elevated MCSs (Marshall et al., 2011). Second, it addresses a common issue in parcel computations of convective available potential energy that have to contend with small layers in which parcel buoyancy goes negative (e.g., similar to the buoyancy in Figure 3c)—this can give rise to an underestimate of the energy actually available to convective storms; the results here indicate why updrafts in large storms easily penetrate such layers.

To briefly summarize the monochromatic dependence on scales: (a) the dependence is nonmonotonic; the horizontal wavelength  $L$  determines the range of nonlocal vertical influence; small  $L$  yields the familiar limit of vertically localized response, while buoyancy layers that are thin compared to  $L/2\pi$  yield response of limited magnitude. (b)  $L$  comparable to or exceeding a substantial fraction of the troposphere depth or of the height of the buoyant layer above the surface yields deep-inflow structure in the lower troposphere.

#### 4. Buoyancy Tartare: Robustness to Fine Structures

Two important modifications occur as one moves from considering a single wavelength to more realistic cases. First, the buoyancy associated with convective updrafts tends to be localized. Features of a finite horizontal size  $D$  and net-positive buoyancy consist of Fourier component contributions from a broad range of wavelength, primarily  $L \gtrsim D$  (Section S4 in Supporting Information S1). This includes nonlocal effects beyond what one would anticipate from the monochromatic considerations above and is in contrast with prior studies that emphasized the contribution from  $L \approx D$  (Jeevanjee, 2017). Second, robustness to complex buoyancy structures associated with imperfectly mixed turbulent flow (Lebo & Morrison, 2015) must be assessed.

To address this, we build net-positive buoyancy patches from an ensemble of smaller elements, using the shorthand “tartare” to describe these constructions of larger scale  $D$  from “minced” ingredients of size  $d \ll D$ . Figures 4a and 4c display two such tartares of diameter  $D \approx 10$  km consisting of warm (red) and cold (blue) bubbles of  $d = 1$  km and depth 0.5 km. In the first set of examples (as in Figure 4a), the tartares are constructed to illustrate the nonlocal influence below the buoyancy by placing them at a distance from the surface. The mean mass flux responses to 10 randomly generated tartares for each  $D$  are demonstrated in Figure 4b (depth indicated by gray shading). Through interference, the integral of individual  $d$ -bubbles leads to primary Fourier contributions from  $L \gtrsim D$  for each  $D$ -tartare (Figure S1 in Supporting Information S1). Thus for larger  $D$  or further below the buoyancy forcing, the responses converge toward linear dependence on height; see also Figure 1c. For smaller  $D$  (e.g.,  $D \approx 5$  km) and closer to the forcing, the vertically localized behaviors—more rapid increase with height near the tartare base—from the smaller-scale  $1 \lesssim L \lesssim 5$  km Fourier components can be distinguished from the nonlocal, roughly linear solutions at lower height ( $z < 2.5$  km) that are dominated by contributions from  $L \gtrsim 5$  km.

Figures 4c and 4d offer additional examples for tilted tartares—to mimic storms under windshear—with a greater depth and lower base. The tilt does not greatly alter the nonlocal behavior for  $D$  exceeding a substantial fraction of the tropospheric depth. Since the tartare base is at  $z = 2$  km, the responses appear roughly linear even for  $D \approx 5$  km. In a more comprehensive setup where the evolution of buoyancy is included, the tilt impacts the location of rain, hence cooling by evaporation of raindrops relative to latent heating. Here, the point is simply that tilted convective systems are subject to the same nonlocal dynamics.

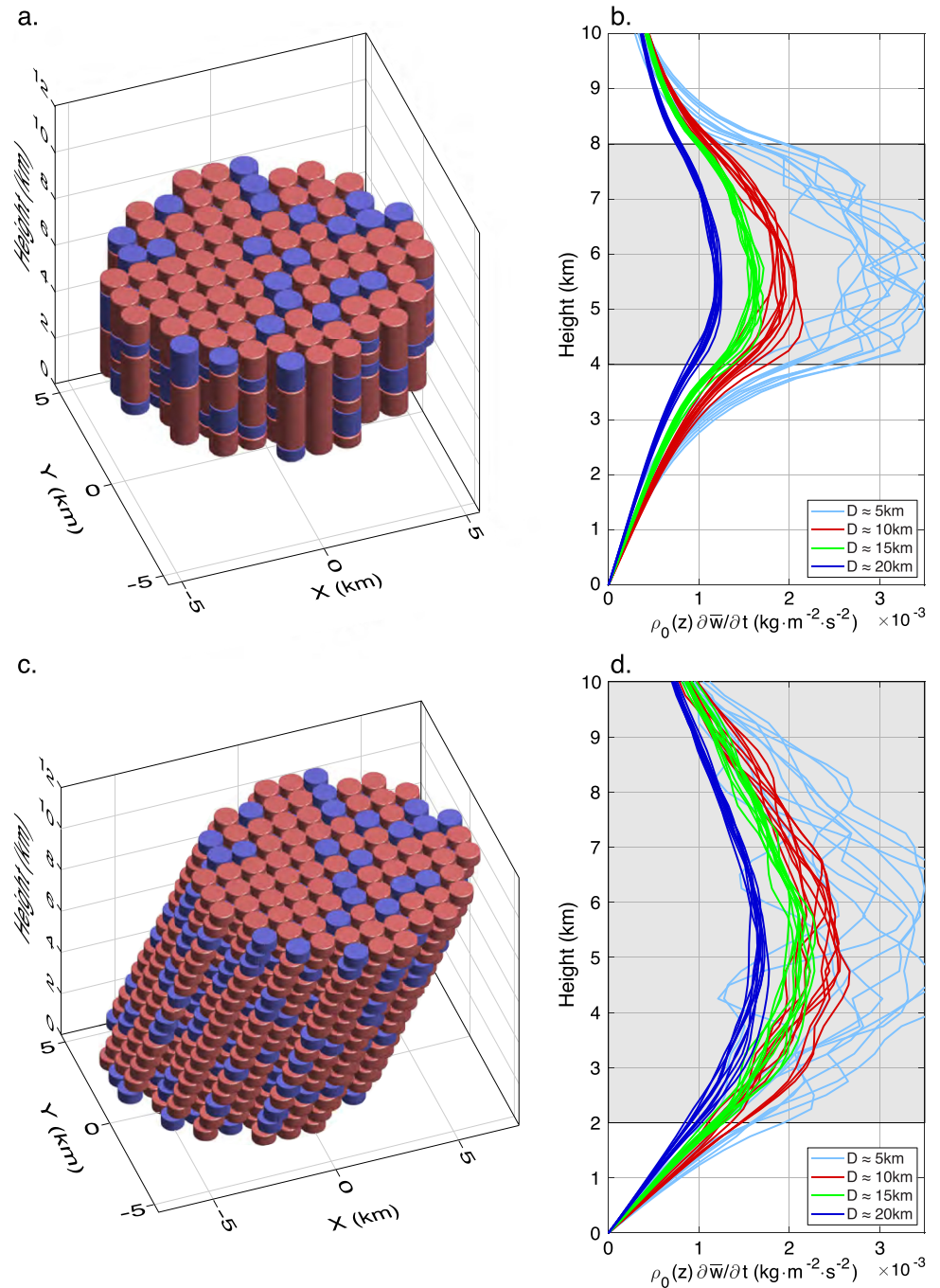


**Figure 4.** (a) A realization of a net-positive buoyancy tartare—an aggregate of stochastically generated smaller positive (red) and negative (blue) buoyancy elements—of horizontal diameter  $D \approx 10$  km and vertical extent  $4 \leq z \leq 8$  km. Buoyancy value within individual element is approximately constant and of equal strength for warm and cold elements. The ratio of numbers of warm to cold elements is set to 7:3. A  $\sim 12$  km region of a 64-km domain is shown. (b) Theoretical response of convective mass flux to an ensemble of 10 tartare realizations as in (a), for varying  $D$ . The average buoyancy over each tartare is rescaled to  $+0.01 \text{ m/s}^2$ . Each curve represents the mean profile within the tartare diameter. (c) As in (a), with vertical extent  $2 \leq z \leq 10$  km and tilt  $\approx 27^\circ$  ( $\Delta z / \Delta x \approx 2$ ). (d) As in (b), but for vertically tilted tartares as in (c). See Section S3 in Supporting Information S1 for numerical details and Figures S2c and S2d in Supporting Information S1 for plume-model comparison.

Compared with idealized bubbles of the same dimensions and constant buoyancy (not shown), the tartare responses are weaker by a small fraction but otherwise exhibit similar profiles. This is consistent with the nonlocal dynamics being robust to small-scale variations and depending primarily on large-scale integral measures for the features of interest. The fine structures within the buoyant region give rise to localized intense accelerations. The effects of this on the horizontal average in Figures 4b and 4d may be seen in variations among instances of the tartare. Below the buoyant region, however, the nonlocal effects create relatively smooth structure even for individual instances. Furthermore, this horizontal-average mass flux is equivalent to the horizontal convergence of air entering the feature, bringing in unmodified air from the far field and thus tending to dominate the effect of the environment on the feature.

## 5. Discussion

Aspects of nonhydrostatic anelastic solutions have been studied in recent years with different focuses. For instance, the rate of entrainment of individual updrafts as a function of updraft size has been examined for dry plumes (Lecoanet & Jeevanjee, 2019). Relationships of entrainment and plume scale have been incorporated into recent convective parameterizations for preliminary testing (Peters et al., 2021). Such approaches are similar to modifying the idealized monochromatic profiles as in Figure 3 as building blocks for constraining mass flux. Although results here are aimed at explaining a feature of observations, they have implications for such parameterization efforts. In particular, they underline that the leading-order flow response to a buoyant region of a finite size includes contributions from a range of wavelengths. This is key to the robustness of nonlocal dynamics at the larger scales involved in convection—those less amenable to treatment by moment closures or traditional turbulent assumptions—especially when one has in mind the formulation for organized ensembles of smaller structures (Moncrieff et al., 2017). The prognostic dynamics also points to the importance of time evolution of convective elements. Superparameterizations include representations of all these effects by partially resolving them with CRMs embedded into GCM grid-boxes (Chern et al., 2016; Jansson et al., 2019; Jones et al., 2019). The nonlocal effects whose importance is emphasized here are thus likely captured, even if small-scale turbulence is not resolved—but superparameterization remains computationally expensive. Approaches such as Morrison (2017) and Lecoanet and Jeevanjee (2019) may be promising if generalized to include the nonlocal effects underlined here both vertically and horizontally. Overall, leveraging anelastic solutions such as those here can help move parameterizations away from the idealization of entrainment as determined purely locally by a parameterized rate.

In light of these results, what can be considered universal regarding the convective mass flux profile? Not so much a specific profile shape, but the inherent vertically and horizontally nonlocal effects tending to yield a deep contribution to the mass flux. The nonlocal dynamics is effective at integrating over heterogeneous buoyancy (as in the tartare solutions) and can generate deep inflow robustly under a wide range of conditions. Variations in the distribution of buoyancy can create departures from this. In particular, a layer of negative buoyancy can yield reductions in the vertical increase of mass flux, or even a low-level layer of negative vertical velocity at small scales. Yet because the nonlocal dynamics operates persistently, deep-inflow profiles tend to appear in averages of mass flux over many convective instances.

The observationally motivated hypothesis that there is a common explanation for the deep inflow into heavily precipitating unorganized convection and mesoscale-organized convection indeed has a simple explanation: the nonlocal dynamics entailing interaction between the buoyant layer and the surface. The robustness of this effect, especially at scales relevant for both large cumulonimbus and MCSs, supports the potential for parameterizing aspects of these systems. Although it implies the need to include nonlocal, anelastic dynamics in convective parameterizations, the overall effect is to simplify key aspects of the interaction with the thermodynamic environment for large convective entities.

## Appendix A: Convective Precipitation Feature Scales and MCS Identification

For convective precipitation features, we use the TRMM 2A25 data (TRMM, 2011) for the period of June 2002 through May 2014 that include PR retrievals of surface rain rate (*rain*) and type (*rainType*) at  $5 \times 5$  km resolution covering  $40^\circ\text{S}$ – $40^\circ\text{N}$ . The values of *rainType* consist of three numerical digits, and here we consider 2X0 ( $X = 0, 2, 3, 4$ ) convective. Note that these are different from shallow-convective and have *rain*  $\geq 0.11$  mm/h—the minimum detectable by the PR. For each 2A25 file (i.e., one orbit), we identify all contiguous areas and/or along-track



chords consisting of convective raining pixels for the two measures of convective feature size. We further associate each area/chord with MCS or non-MCS depending on whether the feature overlaps with an MCS identified following Mohr and Zipser (1996) for simple criteria not directly dependent on precipitation: with the 10.8  $\mu\text{m}$  brightness temperature ( $T_{B_{11}}$ ) from the Merged IR product (Janowiak et al., 2017), for each IR snapshot, we identify MCS as an area with  $T_{B_{11}} < 250$  K of at least 2,000  $\text{km}^2$  and an enclosed minimum  $< 225$  K.

## Data Availability Statement

The TRMM 2A25 (TRMM, 2011) and Merged IR products (Janowiak et al., 2017) are maintained and provided by NASA's GES DISC publicly accessible via <https://disc.gsfc.nasa.gov/>.

## Acknowledgments

This work was supported by National Science Foundation Grant AGS-1936810 and National Oceanic and Atmospheric Administration Grant NA21OAR4310354. We thank J. Meyer-son for graphical assistance.

## References

- Ahmed, F., & Neelin, J. D. (2018). Reverse engineering the tropical precipitation–buoyancy relationship. *Journal of the Atmospheric Sciences*, 75, 1587–1608. <https://doi.org/10.1175/JAS-D-17-0333.1>
- Arakawa, A., & Schubert, W. H. (1974). Interaction of a cumulus cloud ensemble with the large-scale environment, Part I. *Journal of the Atmospheric Sciences*, 31(3), 674–701. [https://doi.org/10.1175/1520-0469\(1974\)031<0674:IOACCE>2.0.CO;2](https://doi.org/10.1175/1520-0469(1974)031<0674:IOACCE>2.0.CO;2)
- Bretherton, C. S., Henn, B., Kwa, A., Brenowitz, N. D., Watt-Meyer, O., McGibbon, J., et al. (2022). Correcting coarse-grid weather and climate models by machine learning from global storm-resolving simulations. *Journal of Advances in Modeling Earth Systems*, 14, e2021MS002794. <https://doi.org/10.1029/2021MS002794>
- Bryan, G. H., & Fritsch, J. M. (2002). A benchmark simulation for moist nonhydrostatic numerical models. *Monthly Weather Review*, 130(12), 2917–2928. [https://doi.org/10.1175/1520-0493\(2002\)130<2917:ABSFMN>2.0.CO;2](https://doi.org/10.1175/1520-0493(2002)130<2917:ABSFMN>2.0.CO;2)
- Burleyson, C. D., Feng, Z., Hagos, S. M., Fast, J., Machado, L. A., & Martin, S. T. (2016). Spatial variability of the background diurnal cycle of deep convection around the GoAmazon2014/5 field campaign sites. *Journal of Applied Meteorology and Climatology*, 55(7), 1579–1598. <https://doi.org/10.1175/jamc-d-15-0229.1>
- Chern, J.-D., Tao, W.-K., Lang, S. E., Matsui, T., Li, J.-L., Mohr, K. I., et al. (2016). Performance of the Goddard multiscale modeling framework with Goddard ice microphysical schemes. *Journal of Advances in Modeling Earth Systems*, 8, 66–95. <https://doi.org/10.1002/2015MS000469>
- Cotton, W. R., Bryan, G. H., & Van den Heever, S. C. (2010). *Storm and cloud dynamics*. Academic Press.
- de Rooy, W. C., & Siebesma, A. P. (2010). Analytical expressions for entrainment and detrainment in cumulus convection. *Quarterly Journal of the Royal Meteorological Society*, 136, 1216–1227. <https://doi.org/10.1002/qj.640>
- Del Genio, A. D., & Wu, J. (2010). The role of entrainment in the diurnal cycle of continental convection. *Journal of Climate*, 23(10), 2722–2738. <https://doi.org/10.1175/2009JCLI3340.1>
- Ferrier, B. S., & Houze, R. A. (1989). One-dimensional time-dependent modeling of GATE cumulonimbus convection. *Journal of the Atmospheric Sciences*, 46, 330–352. [https://doi.org/10.1175/1520-0469\(1989\)046<0330:ODTDMO>2.0.CO;2](https://doi.org/10.1175/1520-0469(1989)046<0330:ODTDMO>2.0.CO;2)
- Gregory, D. (2001). Estimation of entrainment rate in simple models of convective clouds. *Quarterly Journal of the Royal Meteorological Society*, 127(571), 53–72. <https://doi.org/10.1002/qj.49712757104>
- Holloway, C. E., & Neelin, J. D. (2007). The convective cold top and quasi equilibrium. *Journal of the Atmospheric Sciences*, 64(5), 1467–1487. <https://doi.org/10.1175/JAS3907.1>
- Houghton, H. G., & Cramer, H. E. (1951). A theory of entrainment in convective currents. *Journal of the Atmospheric Sciences*, 8(2), 95–102. [https://doi.org/10.1175/1520-0469\(1951\)008<0095:ATOEIC>2.0.CO;2](https://doi.org/10.1175/1520-0469(1951)008<0095:ATOEIC>2.0.CO;2)
- Houze, R. A. (1993). *Cloud dynamics*. Academic Press.
- Janowiak, J., Joyce, B., & Xie, P. (2017). NCEP/CPC L3 half hourly 4km global (60S–60N) Merged IR V1. In A. Savtchenko (Ed.), Goddard Earth Sciences Data and Information Services Center. <https://doi.org/10.5067/P4HZB9N27EKU>
- Jansson, F., vanden Oord, G., Pelupessy, I., Grönqvist, J. H., Siebesma, A. P., & Crommelin, D. (2019). Regional superparameterization in a global circulation model using large eddy simulations. *Journal of Advances in Modeling Earth Systems*, 11, 2958–2979. <https://doi.org/10.1029/2018MS001600>
- Jeevanjee, N. (2017). Vertical velocity in the gray zone. *Journal of Advances in Modeling Earth Systems*, 9, 2304–2316. <https://doi.org/10.1002/2017MS001059>
- Jeevanjee, N., & Romps, D. M. (2016). Effective buoyancy at the surface and aloft. *Quarterly Journal of the Royal Meteorological Society*, 142(695), 811–820. <https://doi.org/10.1002/qj.2683>
- Jones, T. R., Randall, D. A., & Branson, M. D. (2019). Multiple-instance superparameterization: 1. Concept, and predictability of precipitation. *Journal of Advances in Modeling Earth Systems*, 11, 3497–3520. <https://doi.org/10.1029/2019MS001610>
- Jung, J.-H., & Arakawa, A. (2008). A three-dimensional anelastic model based on the vorticity equation. *Monthly Weather Review*, 136(1), 276–294. <https://doi.org/10.1175/2007MWR2095.1>
- Khairoutdinov, M. F., & Randall, D. A. (2003). Cloud resolving modeling of the arm summer 1997 IOP: Model formulation, results, uncertainties, and sensitivities. *Journal of the Atmospheric Sciences*, 60(4), 607–625. [https://doi.org/10.1175/1520-0469\(2003\)060<0607:CRMOTA>2.0.CO;2](https://doi.org/10.1175/1520-0469(2003)060<0607:CRMOTA>2.0.CO;2)
- Kuang, Z., & Bretherton, C. S. (2006). A mass-flux scheme view of a high-resolution simulation of a transition from shallow to deep cumulus convection. *Journal of the Atmospheric Sciences*, 63, 1895–1909. <https://doi.org/10.1175/JAS3723.1>
- Kuo, Y.-H., Neelin, J. D., Booth, J. F., Chen, C.-C., Chen, W.-T., Gettelman, A., et al. (2020). Convective transition statistics over tropical oceans for climate model diagnostics: GCM evaluation. *Journal of the Atmospheric Sciences*, 77, 379–403. <https://doi.org/10.1175/JAS-D-19-0132.1>
- Lebo, Z., & Morrison, H. (2015). Effects of horizontal and vertical grid spacing on mixing in simulated squall lines and implications for convective strength and structure. *Monthly Weather Review*, 143(11), 4355–4375. <https://doi.org/10.1175/MWR-D-15-0154.1>
- Lecoanet, D., & Jeevanjee, N. (2019). Entrainment in resolved, dry thermals. *Journal of the Atmospheric Sciences*, 76(12), 3785–3801. <https://doi.org/10.1175/JAS-D-18-0320.1>
- LeMone, M. A., & Zipser, E. J. (1980). Cumulonimbus vertical velocity events in GATE. Part I: Diameter, intensity and mass flux. *Journal of the Atmospheric Sciences*, 37(11), 2444–2457. [https://doi.org/10.1175/1520-0469\(1980\)037<2444:CVVEIG>2.0.CO;2](https://doi.org/10.1175/1520-0469(1980)037<2444:CVVEIG>2.0.CO;2)

- Leung, L. R., Boos, W. R., Catto, J. L., DeMott, C., Martin, G. M., Neelin, J. D., et al. (2022). Exploratory precipitation metrics: Spatiotemporal characteristics, process-oriented, and phenomena-based. *Journal of Climate*, *35*(12), 3659–3686. <https://doi.org/10.1175/JCLI-D-21-0590.1>
- Li, Y., Zipser, E. J., Krueger, S. K., & Zulauf, M. A. (2008). Cloud-resolving modeling of deep convection during KWAJEX. Part I: Comparison to TRMM satellite and ground-based radar observations. *Monthly Weather Review*, *136*(7), 2699–2712. <https://doi.org/10.1175/2007MWR2258.1>
- Lucas, C., Zipser, E. J., & Lemone, M. A. (1994). Vertical velocity in oceanic convection off tropical Australia. *Journal of the Atmospheric Sciences*, *51*(21), 3183–3193. [https://doi.org/10.1175/1520-0469\(1994\)051<3183:VVIOCO>2.0.CO;2](https://doi.org/10.1175/1520-0469(1994)051<3183:VVIOCO>2.0.CO;2)
- Markowski, P., & Richardson, Y. (2011). *Mesoscale meteorology in midlatitudes* (Vol. 2). John Wiley & Sons.
- Marshall, J. H., Trier, S. B., Weckwerth, T. M., & Wilson, J. W. (2011). Observations of elevated convection initiation leading to a surface-based squall line during 13 June IHOP\_2002. *Monthly Weather Review*, *139*(1), 247–271. <https://doi.org/10.1175/2010MWR3422.1>
- Masunaga, H., & Luo, Z. J. (2016). Convective and large-scale mass flux profiles over tropical oceans determined from synergistic analysis of a suite of satellite observations. *Journal of Geophysical Research: Atmospheres*, *121*, 7958–7974. <https://doi.org/10.1002/2016JD024753>
- Mohr, K. I., & Zipser, E. J. (1996). Mesoscale convective systems defined by their 85-GHz ice scattering signature: Size and intensity comparison over tropical oceans and continents. *Monthly Weather Review*, *124*, 2417–2437. [https://doi.org/10.1175/1520-0493\(1996\)124<2417:MCSDBT>2.0.CO;2](https://doi.org/10.1175/1520-0493(1996)124<2417:MCSDBT>2.0.CO;2)
- Moncrieff, M. W., Liu, C., & Bogenschutz, P. (2017). Simulation, modeling, and dynamically based parameterization of organized tropical convection for global climate models. *Journal of the Atmospheric Sciences*, *74*(5), 1363–1380. <https://doi.org/10.1175/JAS-D-16-0166.1>
- Moncrieff, M. W., Waliser, D. E., Miller, M. J., Shapiro, M. A., Asrar, G. R., & Caughey, J. (2012). Multiscale convective organization and the YOTC virtual global field campaign. *Bulletin of the American Meteorological Society*, *93*(8), 1171–1187. <https://doi.org/10.1175/BAMS-D-11-00233.1>
- Morrison, H. (2016). Impacts of updraft size and dimensionality on the perturbation pressure and vertical velocity in cumulus convection. Part I: Simple, generalized analytic solutions. *Journal of the Atmospheric Sciences*, *73*(4), 1441–1454. <https://doi.org/10.1175/JAS-D-15-0040.1>
- Morrison, H. (2017). An analytic description of the structure and evolution of growing deep cumulus updrafts. *Journal of the Atmospheric Sciences*, *74*(3), 809–834. <https://doi.org/10.1175/JAS-D-16-0234.1>
- Nesbitt, S., Cifelli, W. R., & Rutledge, S. A. (2006). Storm morphology and rainfall characteristics of TRMM precipitation features. *Monthly Weather Review*, *134*, 2702–2721. <https://doi.org/10.1175/MWR3200.1>
- Ogura, Y., & Phillips, N. A. (1962). Scale analysis of deep and shallow convection in the atmosphere. *Journal of the Atmospheric Sciences*, *19*(2), 173–179. [https://doi.org/10.1175/1520-0469\(1962\)019<0173:SAODAS>2.0.CO;2](https://doi.org/10.1175/1520-0469(1962)019<0173:SAODAS>2.0.CO;2)
- Peters, J. M. (2016). The impact of effective buoyancy and dynamic pressure forcing on vertical velocities within two-dimensional updrafts. *Journal of the Atmospheric Sciences*, *73*(11), 4531–4551. <https://doi.org/10.1175/JAS-D-16-0016.1>
- Peters, J. M., Morrison, H., Zhang, G., & Powell, S. W. (2021). Improving the physical basis for updraft dynamics in deep convection parameterizations. *Journal of Advances in Modeling Earth Systems*, *13*, e2020MS002282. <https://doi.org/10.1029/2020MS002282>
- Plant, R. S. (2010). A review of the theoretical basis for bulk mass flux convective parameterization. *Atmospheric Chemistry and Physics*, *10*(8), 3529–3544. <https://doi.org/10.5194/acp-10-3529-2010>
- Robe, F. R., & Emanuel, K. A. (1996). Moist convective scaling: Some inferences from three-dimensional cloud ensemble simulations. *Journal of the Atmospheric Sciences*, *53*, 3265–3275. [https://doi.org/10.1175/1520-0469\(1996\)053<3265:MCSSEIF>2.0.CO;2](https://doi.org/10.1175/1520-0469(1996)053<3265:MCSSEIF>2.0.CO;2)
- Romps, D. M. (2010). A direct measure of entrainment. *Journal of the Atmospheric Sciences*, *67*(6), 1908–1927. <https://doi.org/10.1175/2010JAS3371.1>
- Savazzi, A. C., Jakob, C., & Siebesma, A. P. (2021). Convective mass-flux from long term radar reflectivities over Darwin, Australia. *Journal of Geophysical Research: Atmospheres*, *126*, e2021JD034910. <https://doi.org/10.1029/2021JD034910>
- Schiro, K. A., Ahmed, F., Giangrande, S. E., & Neelin, J. D. (2018). GoAmazon2014/5 campaign points to deep-inflow approach to deep convection across scales. *Proceedings of the National Academy of Sciences of the United States of America*, *115*(18), 4577–4582. <https://doi.org/10.1073/pnas.1719842115>
- Sherwood, S. C., Bony, S., & Dufresne, J.-L. (2014). Spread in model climate sensitivity traced to atmospheric convective mixing. *Nature*, *505*(7481), 37. <https://doi.org/10.1038/nature12829>
- Siebesma, A. P., Bretherton, C. S., Brown, A., Chlond, A., Cuxart, J., Duynkerke, P. G., et al. (2003). A large eddy simulation intercomparison study of shallow cumulus convection. *Journal of the Atmospheric Sciences*, *60*(10), 1201–1219. [https://doi.org/10.1175/1520-0469\(2003\)60<1201:ALESIS>2.0.CO;2](https://doi.org/10.1175/1520-0469(2003)60<1201:ALESIS>2.0.CO;2)
- Siebesma, A. P., Soares, P. M. M., & Teixeira, J. (2007). A combined eddy diffusivity mass flux approach for the convective boundary layer. *Journal of the Atmospheric Sciences*, *64*, 1230–1248. <https://doi.org/10.1175/JAS3888.1>
- Trapp, R. J. (2013). *Mesoscale-convective processes in the atmosphere*. Cambridge University Press.
- TRMM. (2011). *TRMM precipitation radar rainfall rate and profile L2 1.5 hours V7*. Goddard Earth Sciences Data and Information Services Center. Retrieved from [https://disc.gsfc.nasa.gov/datacollection/TRMM\\_2A25\\_7.html](https://disc.gsfc.nasa.gov/datacollection/TRMM_2A25_7.html)
- Wing, A. A., Stauffer, C. L., Becker, T., Reed, K. A., Ahn, M.-S., Arnold, N. P., et al. (2020). Clouds and convective self-aggregation in a multimodel ensemble of radiative-convective equilibrium simulations. *Journal of Advances in Modeling Earth Systems*, *12*, e2020MS002138. <https://doi.org/10.1029/2020MS002138>
- Yano, J.-I., & Moncrieff, M. W. (2016). Numerical archetypal parameterization for mesoscale convective systems. *Journal of the Atmospheric Sciences*, *73*(7), 2585–2602. <https://doi.org/10.1175/JAS-D-15-0207.1>
- Yano, J.-I., & Plant, R. S. (2020). Why does Arakawa and Schubert's convective quasi-equilibrium closure not work? Mathematical analysis and implications. *Journal of the Atmospheric Sciences*, *77*(4), 1371–1385. <https://doi.org/10.1175/JAS-D-19-0165.1>